journal of the mechanical behavior of biomedical materials 111 (2020) 104005

Contents lists available at ScienceDirect

Journal of the Mechanical Behavior of Biomedical Materials

journal homepage: http://www.elsevier.com/locate/jmbbm

Improving stress corrosion cracking behavior of AZ31 alloy with conformal thin titania and zirconia coatings for biomedical applications

M. Peron *, A. Bin Afif, A.L. Dadlani, F. Berto, J. Torgersen

Department of Industrial and Mechanical Engineering, Norwegian University of Science and Technology, Richard Birkelands vei 2b, 7034, Trondheim, Norway

ARTICLE INFO

Keywords:
Stress corrosion cracking (SCC)
Biomedical applications
Magnesium alloys
Thin films
Atomic layer deposition (ALD)

ABSTRACT

Magnesium and its alloys have been widely studied as materials for temporary implant devices. However, corrosion-assisted cracking phenomena such as stress corrosion cracking (SCC) continue to prevent their mainstream use. For the first time, we explore the SCC susceptibility of Atomic Layer Deposition (ALD) coated AZ31 alloys in Simulated Body Fluid (SBF). Conformal 100 nm coatings of titania and zirconia were deposited on standard dogbone specimens and subjected to slow strain rate tests at 3.5 10^{-6} s^{-1} and a temperature of 37 °C. Remarkably, the SCC susceptibility index I_{UTS} was reduced by 6% and 40% and the I_ε was reduced by more than 70% and 76% with a titania and zirconia coating, respectively. Potentiodynamic polarization, hydrogen evolution and fracture behavior of the samples revealed the drastic corrosion reduction to be the main reason for the susceptibility reduction. We discuss the observed SCC behavior of our samples in light of the coatings' electrochemical activities, wettabilities, surface integrities and mechanical properties. This straightforward conformal surface treatment can be useful as a workaround for one of the major bottlenecks of biomedical Mg based implants and hence provides a possible pathway for making them more commonplace in the field.

1. Introduction

The number of orthopedic surgeries is continuously increasing (Ginebra et al., 2006; http://share.iofbonehealt). However, common implant materials are affected by two main issues, i.e. 1) the stress-shielding phenomenon as a consequence of the materials' elastic modulus difference to human bone (Bauer and Schils, 1999; Dujovne et al., 1993; Engh and Bobyn, 1988; Kerner et al., 1999; Sumner and Galante, 1992; Turner et al., 1997; Van Rietbergen et al., 1993; Wolff, 1986) and 2) the risk of long-term complications such as inflammations and secondary surgeries (Pound, 2014a, 2014b; Jacobs et al., 1998, 2003; Beech et al., 2006). The mechanical compatibility to bone renders Magnesium (Mg) and its alloys excellent implant material alternatives (Singh Raman et al., 2015; Peron et al., 2017; Staiger et al., 2006; Hänzi et al., 2009), especially in light of their high biocompatibility. Mg is in fact highly abundant in the human body (Staiger et al., 2006), is essential for the metabolism in many biological mechanisms, is a cofactor for many enzymes (Hänzi et al., 2009), and Mg^{2+} ions resulting from the degradation process are reported to aid the healing process and the growth of tissue (Peron et al., 2020a). However, their application as load bearing implant material is still not clinically accepted (Peron et al., 2020b; Wang et al., 2020). High corrosion rates reduce their compatible properties prematurely, before a respective device can accomplish its defined mission (Song, 2007). Furthermore, alkalization and accumulation of hydrogen pockets next to the implant can cause the necrosis of tissues. It is a necessity to reduce the corrosion rate of load bearing Mg implants to a level where hydrogen evolution and alkalization can be balanced by metabolic mechanisms. However, this challenge cannot be tackled by tailoring the chemical compatibility only. The implant must also possess adequate resistance to cracking under the simultaneous action of the corrosive environment and mechanical load. In this way, corrosion-assisted cracking phenomena, such as stress corrosion cracking (SCC), are already a challenge for non-degradable implant materials in clinical applications (Teoh, 2000; Akahori et al., 2000; Jafari et al., 2015; Antunes and de Oliveira, 2012) and are expected to be of even bigger concern if the implant material is intended to degrade (Jafari et al., 2017, 2018; Kannan and Raman, 2008). It is thus important to develop Mg-based implants that confer a combination of strength and corrosion resistance in physiologically relevant environments such as Simulated Body Fluid (SBF).

Whereas corrosion mitigation of Mg materials is a common research topic (Qi et al., 2014; Zhen et al., 2014; Hou et al., 2012), the literature

* Corresponding author.
E-mail address: mirco.peron@ntnu.no (M. Peron).

https://doi.org/10.1016/j.jmbbm.2020.104005
Received 11 April 2020; Received in revised form 19 July 2020; Accepted 21 July 2020
Available online 27 July 2020

on their resistance to SCC is yet scarce (Peron et al., 2020c). For example, Mohajernia et al. (2018) reported that hydroxyapatite coatings containing multi-walled carbon nanotubes reduce the corrosion current density of AZ31 alloys in SBF at 37 °C by three orders of magnitude. The elongation to failure (ε_f) of AZ31 increased by ~70% under slow strain rate tests (SSRT). Chen et al. (2018) coated Mg–4Zn-0.6Zr-0.4Sr with a composite coating consisting of a poly (lactic-co-glycolic acid) on a micro-arc oxidated (MAO) layer on the substrate. They reported an increase in the ε_f in modified SBF by ~120% as compared to the bare alloy. The application of coatings seems promising for SCC susceptibility reduction. However, the reported coating technologies have limitations in line of sight (Smith, 2007), conformality, process inherent density (Lei, 2015) and biocompatibility (Sonia and Sharma, 2014) as well as limited controllability of the thickness (Li, 2013).

Atomic Layer Deposition (ALD) does not have these limitations. It yields thin films with high conformality, uniformity and a thickness controllable on the atomic level (Cremers et al., 2019). Recently, it has been explored for corrosion protection (Graniel et al., 2018; Chalker, 2016), where, for example, a 100 nm thick TiO_2 and ZrO_2 layer reduced the corrosion current density of a commercial AZ31 Mg alloy by two orders of magnitude (Marin et al., 2012) and three orders of magnitude (Liu et al., 2018), respectively. Interestingly, the corrosion protection of ALD coated AZ31 samples was found to be much higher than that of sputter coated AZ31 counterparts, especially when considering complex 3D substrates (Peron et al., 2020d).

To the best of our knowledge, the effect of ALD coatings on the SCC susceptibility is yet underexplored. Promising preliminary results were published by the authors (Peron et al., 2019a, 2019b), yet no thorough investigation has been performed. Here, we explore the SCC susceptibility of AZ31 alloy coated with a 100 nm thick ALD ZrO_2 and TiO_2 layers, where ZrO_2 and TiO_2 were chosen as coating materials due to their known biocompatibility (Kasuga et al., 2002; Wang et al., 2002; Uchida et al., 1999; Harianawala, Kheur, Kheur, Sethi, Bal, Burhanpurwala, Sayed; Rimondini, Cerroni, Carrassi, Torricelli). SSRTs at strain rate 3.5 10^{-6} s^{-1} were carried out while immersing the samples in SBF at physiological temperature (37 °C) for the whole duration of the tests. The corrosion behavior was investigated through potentiodynamic polarization curves and hydrogen evolution experiments. The mechanisms of SCC susceptibility reduction were further discussed through fracture surfaces after SSRTs.

2. Materials and methods

2.1. Materials and environment

AZ31 Mg alloy was supplied in the form of commercially available bars. The microstructure of the material in the as-received condition is shown in Fig. 1 and consists of a quite homogeneous α matrix. The initial grain size was measured by the linear intercept method resulting in sizes of 13.2 ± 8 μm.

The test medium was a simulated body fluid (SBF) prepared according to Ref. (Kokubo and Takadama, 2006).

2.2. Atomic Layer Deposition

The deposition of the ALD coatings was performed in a commercial ALD reactor (Savannah S200, Veeco Instruments Inc., Massachusetts, USA) through successive cyclic reactions. 926 successive cycles of ZrO_2 utilizing Tetrakis (dimethylamino) zirconium (TDMAZ) and deionized water (H_2O) as reactants were carried out at 160 °C to obtain a total thickness of 100 nm. Each cycle was composed of two parts. The first part consisted of a 250-ms TDMAZ precursor pulse and a 10-s Hi-purity N_2 purge (semiconductor grade) with a flow rate of 20 sccm to remove residual reactants and by-products from the chamber to separate the chemical vapor deposition reactions. The second part comprised a 150-ms H_2O precursor pulse and a 15-ms High-purity N_2 purge. In the process of deposition, the TDMAZ precursor and delivery lines were heated to 75 °C and 160 °C, respectively, while the H_2O precursor was kept at room temperature. During the deposition process, the ZrO_2 layer deposition rate was of approximately 1.08 Å/cycle. Concerning TiO_2, the metal organic precursor used was Tetrakis (dimethylamido) titanium (IV) (TDMA-Ti) heated to 75 °C. Each cycle was composed of two parts. The first part consisted of a 0.1 s TDMA-Ti precursor pulse and a 5 s High-purity N_2 purge with a flow rate of 20 sccm. The second part comprised a 0.015 s H_2O precursor pulse and a 5 s High-purity N_2 purge. The deposition rate was found to be 0.5 Å/cycle.

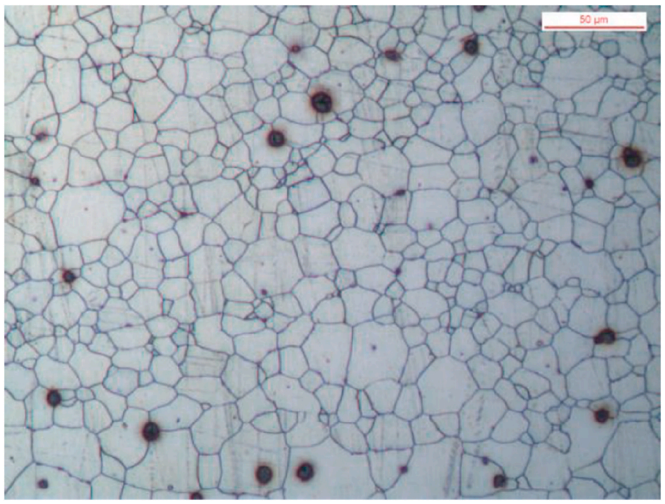

Fig. 1. Microstructure of the AZ31 alloy in the as-received condition.

2.3. Coating characterization

The film thickness was determined using spectroscopic ellipsometry (J.A. Woollam M2000U, Lincoln, United States) at a fixed angle of incidence of 65°. The measurements were conducted on thin films deposited on p-doped <100> 500 μm thick, 2 inch Si wafer. A Si wafer per each coating material was put inside the ALD reactor during the deposition on the Mg substrates. The ellipsometer data were fitted using a B-spline model with Si substrate, a native oxide layer and the ALD layer of the required material.

X-ray photoelectron spectroscopy (XPS) measurements were conducted to assess the chemical composition of the TiO_2, and ZrO_2 coating. Kratos Analytical XPS Microprobe (Kratos Analytical Ltd, Manchester, UK) which uses Al (Kα) radiation of 1486 eV in a vacuum environment of $5*10^{-9}$ Torr was used. CasaXPS software was used to analyze the XPS data.

In addition, the surface integrity (amount and length of cracks) of TiO_2, and ZrO_2 coated discs (geometrical details are reported in Section 2.4.) was analyzed using FEI Quanta 450 Scanning electron Microscope (Thermo Fisher Scientific Inc., USA) with an acceleration voltage of 10 kV at a working distance of about 10 mm. Three samples for each respective condition were assessed for reproducibility.

2.4. Potentiodynamic polarization curves

Discs with a diameter of 29 mm and a thickness of 2 mm were manufactured using a lathe from the commercially available bars. The samples were then grounded with 2000 grit silicon carbide papers and cleaned with acetone and ethanol for 5 min in an ultrasonic bath. Fifteen samples were then coated as described in Section 2.2. Potentiodynamic polarization curves of bare and coated samples were carried out in simulated body fluid (SBF) with a pH of 7.4 on a Gamry Reference 600+ potentiostat. As common practice in literature (Cai et al., 2019), the electrochemical tests used a three-electrode equipment with the bare or

coated samples as a working electrode, a Hg/Hg_2SO_4 electrode as a reference electrode, and a platinum plate as counter electrode, respectively. The area of the samples exposed to SBF was 1 cm^2 (excluding roughness induced area deviations). The potentiodynamic polarization tests were conducted at a stable open-circuit potential after a stabilization period of 30 min. The scan rate of the potentiodynamic polarization test was 0.5 mV/s.

2.5. Hydrogen evolution tests

Hydrogen evolution experiments were carried out according to ref (Song et al., 2013). Cubic samples of 5 mm side lengths were obtained from the as-received material, were grounded with 2000 grit silicon carbide paper and cleaned with acetone and ethanol for 5 min in ultrasonic bath. Five samples were then coated as described in Section 2.2. The immersion tests were carried out in SBF at 37 °C for 7 days individually to monitor the hydrogen evolution. Hydrogen bubbles were collected in a burette from each sample.

2.6. Slow strain rate tests (SSRT)

Cylindrical dog-bone-shaped samples, with dimensions reported in Fig. 2, were tested according to a standard (ASTM International, ASTM-E466-96). The samples were machined from the received bars using a lathe.

The samples were then ground with 2000 grit silicon carbide papers and cleaned with acetone and ethanol for 5 min in ultrasonic bath. Fifteen samples were then coated as described in Section 2.2.

The SSRTs were carried out both on bare, TiO_2 and ZrO_2 coated samples, respectively at a strain rate of $3.5{\cdot}10^{-6}$ s^{-1} in SBF solution held at physiologically relevant temperatures (37 ± 1 °C). The strain rate was chosen to render the Mg alloy susceptible to SCC (Bobby Kannan et al., 2008). A schematic representation of the experimental set-up is shown in Fig. 3. The sample was immersed for the whole duration of the test and the SBF was constantly changed with a pumping system. The SBF container was immersed in a water bath, where temperature was controlled. While carrying out the SSRTs, the area of the specimen exposed to SBF was restricted to its gauge length by using Teflon tapes wrapped around the rest of the specimen maintaining a constant area of exposure to the corrosive solution as well as avoiding the possibility of galvanic effects with other components of the testing set-up.

In order to quantify the AZ31 SCC sensitivity, the susceptibility indices I_{UTS} and I_ε were calculated according to Eq. (1) and Eq. (2) (Choudhary et al., 2014):

$$I_{UTS} = \frac{UTS_{air} - UTS_{SBF}}{UTS_{air}} \quad (1)$$

$$I_\varepsilon = \frac{\varepsilon_{air} - \varepsilon_{SBF}}{\varepsilon_{air}} \quad (2)$$

where UTS is the Ultimate Tensile Strength and ε the elongation at

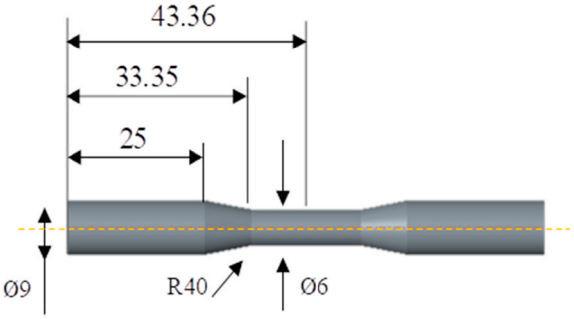

Fig. 2. Geometry and dimensions of the samples for SSRTs.

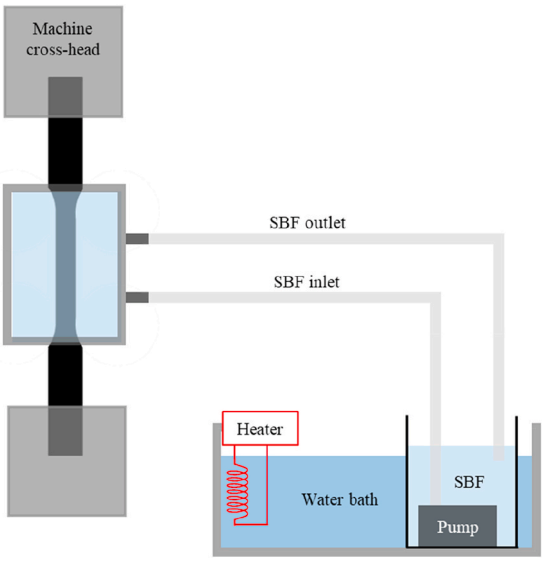

Fig. 3. Schematic representation of the SSRT set-up.

failure both evaluated during tests conducted in SBF and air. When the value of the susceptibility index approaches zero, the material is considered to be highly resistant to SCC, namely the greater the index the greater the susceptibility to SCC.

2.7. Fractography

The specimen fracture surfaces after SSRTs were cleaned by immersion for 1 min in a solution prepared using 50 g chromium trioxide (CrO_3), 2.5 g silver nitrate ($AgNO_3$) and 5 g barium nitrate ($Ba(NO_3)_2$) in 250 ml distilled water, as suggested by (Thirumalaikumarasamy et al., 2014). The specimens were then washed with distilled water and finally ultrasonically cleaned in acetone for 10 min. The fracture surfaces were observed by means of a FEI™ QUANTA 450 SEM (Thermo Fisher Scientific Inc., USA).

3. Results

3.1. Coating characterization

3.1.1. Ellipsometer and XPS analyses

Spectroscopic ellipsometry at a fixed angle of incidence of 65° was conducted to determine the thickness of the deposited coatings. The measurements were carried out on Si wafers coated in the same deposition process of the Mg substrates, and the results reported the TiO_2 and ZrO_2 coatings to be 100.98 and 100.97 nm thick, respectively.

XPS was instead conducted to determine the chemical composition of the ALD deposited TiO_2 and ZrO_2. The measurements were carried out on thin films deposited on p-doped <100> 500 μm thick, 2 inch Si wafers, in order to have minimum effect of the underlying substrate. To start with, etching was conducted on the surface to remove the effect of environmental contamination and surface oxidation. Surface was etched for 180 s with an energy of 2 KeV. On TiO_2 substrates, regional scans for Ti 2p, O 1s and C 1s were carried out at high resolution. Negligible amounts of C were observed in the regional scan indicating an ideal deposition without any process contamination. Fig. 4 (a) and (b) are regional scan of Ti 2p and O 1s, respectively. For Ti, peaks corresponding to the core level binding energies, 459 eV and 464 eV of Ti $2p_{3/2}$ and Ti $2p_{1/2}$ are observed, which is due to Ti^{4+} oxidation state in TiO_2 (Nezar et al., 2017). The shoulder at lower energy around 456 eV is due to the presence of Ti^{3+} caused by the argon etching step (Kim et al., 1999). The O peak at 531 eV is related to O atoms in TiO_2 phase (Yu et al., 2000), while the small shoulder at higher energy is due to O in OH groups

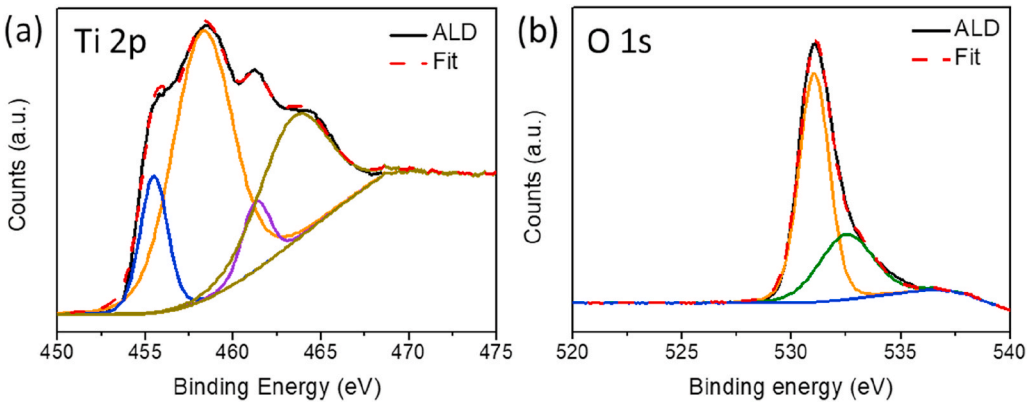

Fig. 4. XPS spectra for ALD deposited TiO_2 (a) Ti 2p (b) O 1s.

present in the form impurities. Stoichiometric TiO_2 thin films should have Ti and O in 1:2 ratio i.e. 66.7% oxygen and 33.3% titanium, but in our case, we have found the composition to be around 60% for oxygen and 40% titanium, thus indicating an oxygen deficient deposition.

Regional scans of Zr 3d, O 1s and C 1s were also carried out for ZrO_2 coated samples at high resolution. No peak was observed in the high-resolution scan for elemental carbon indicating a carbon free ALD deposition. The high-resolution spectra (Fig. 5a) of Zr 3d shows two peaks at binding energy 182 eV and 184 eV, which correspond to Zr $3d_{5/2}$ and Zr $3d_{3/2}$, respectively. The scan conducted for O 1s (Fig. 5b) showed a peak at 530 eV which belongs to ZrO_2 and the shoulder on the higher energy side is due to the oxidation of metal in air forming ZrO. The quantification calculation using CASA XPS software showed a composition as 40% Zr and 60% O. This indicates an oxygen deficient ZrO_2 thin film.

3.1.2. Surface integrity

The presence of cracks on TiO_2 and ZrO_2 coated samples have been assessed by means of SEM analyses and the representative images have been reported in Fig. 6. In addition, the average length and numerosity are reported in Table 1.

It can be noted that the number of cracks (crack density in Table 1) and the length of the cracks increased moving from ZrO_2 to TiO_2 coated samples.

3.2. Potentiodynamic polarization curves

The potentiodynamic polarization curves of the TiO_2 and ZrO_2 coated and bare samples are shown in Fig. 7 and the results of the corrosion potentials (E_{corr}) and of the corrosion current densities (i_{corr}) are shown in Table 2. Compared to the uncoated alloy, the corrosion current densities of the coated samples display declining trends (Fig. 7 and Table 2). In particular, the ZrO_2 coating is shown to provide a higher reduction of the corrosion current density compared to the TiO_2 coating. Since a lower corrosion current density corresponds to a smaller corrosion rate, this suggests that the application of coatings protects Mg alloys from corrosion, which is consistent with previous reports (Liu et al., 2011, 2018; Yang et al., 2017). In particular, the increased protectiveness after the application of coatings is reported to be linked to their barrier properties (Huang et al., 2019).

3.3. Hydrogen evolution tests

The hydrogen evolution curves of bare and coated samples are reported in Fig. 8, and the results further suggest that the application of coatings can prevent the degradation of AZ31 alloy. In particular, the 100 nm thick ZrO_2 coating provides a better protection than the TiO_2 coating. The hydrogen evolved from the bare sample is in fact reduced by 93% with a ZrO_2 coating and by 52% with a TiO_2 coating, respectively.

3.4. Slow strain rate tests (SSRT)

The engineering stress-strain curves for the bare, TiO_2 coated and ZrO_2 coated AZ31 samples tested in air and in SBF are reported in Fig. 9 a, b and c respectively. In addition, Table 3 compares the UTS and elongation at failure values obtained from the curves in Fig. 9.

The surface characteristics did not influence the AZ31 mechanical properties when tested in air. Both the bare and the coated samples are characterized by an excellent and comparable combination of strength and ductility. On the other hand, the coated samples were characterized by a considerably higher elongation to failure than the bare counterparts

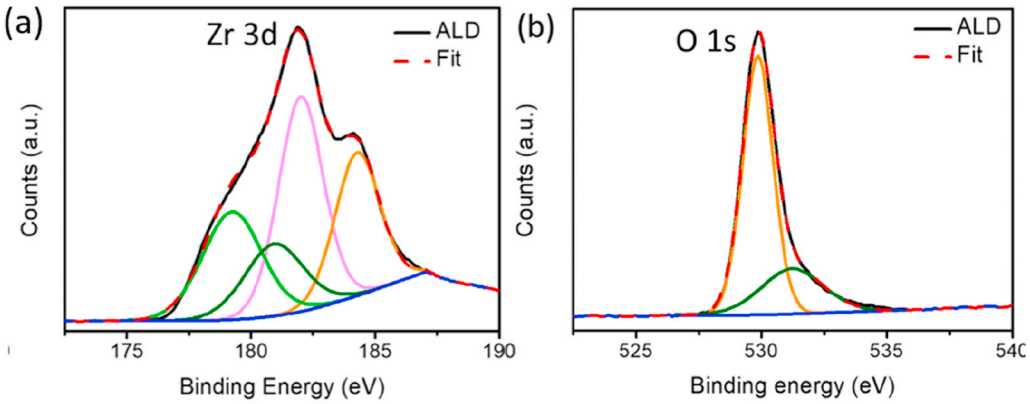

Fig. 5. XPS spectra for ALD deposited ZrO_2 (a) Zr 3d (b) O 1s.

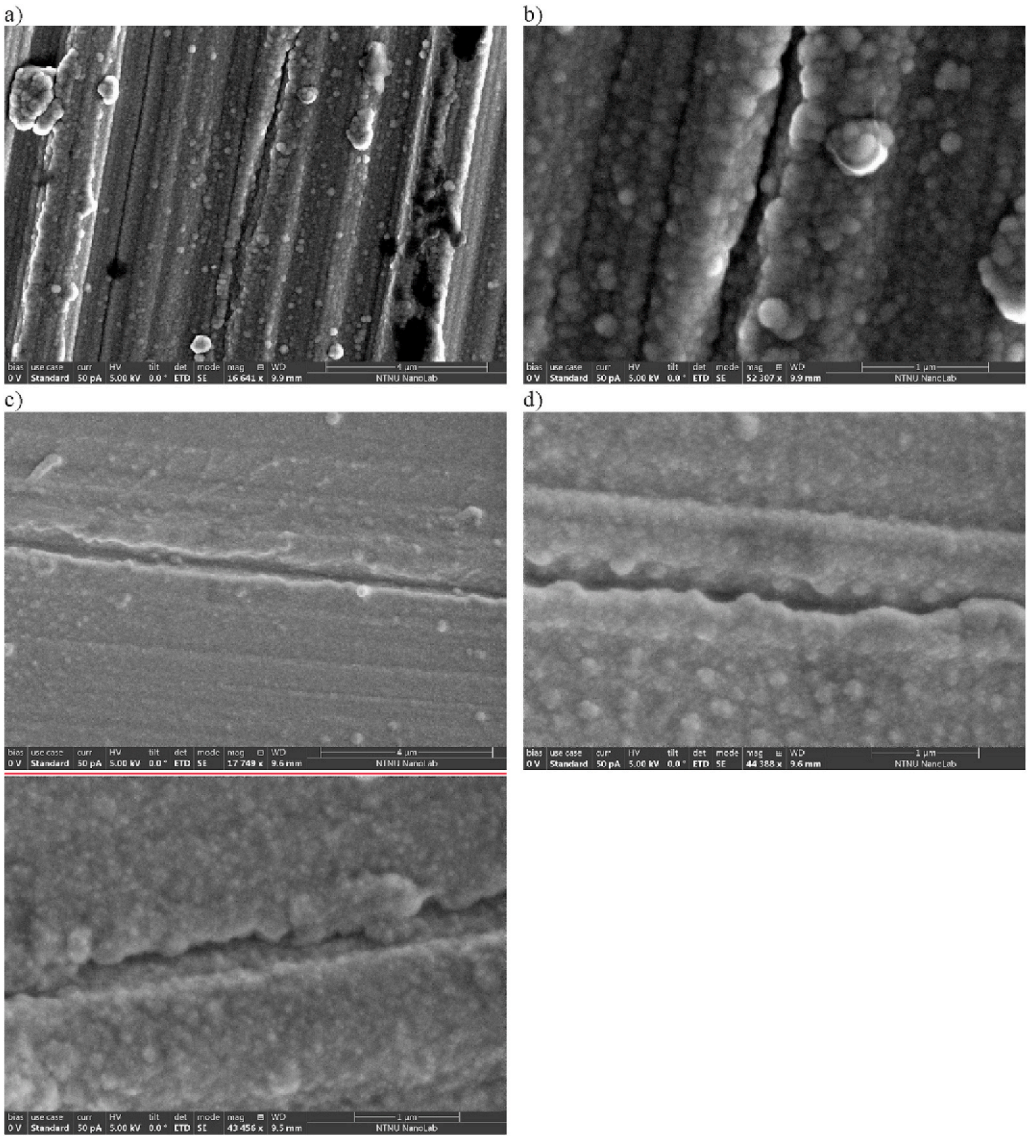

Fig. 6. SEM images of representative cracks formed on TiO_2 coated (a and b) and ZrO_2 coated discs (c and d).

Table1
Average crack length and density (meant as number of cracks per square centimetre) of the cracks detected for the different conditions.

	TiO_2	ZrO_2
Crack length (μm)	4.54 ± 3.05	3.14 ± 2.41
Density (n° cracks/cm²)	0.87 ± 0.37	0.61 ± 0.28

when tested in SBF, indicating a lower tendency to suffer from embrittlement in SBF. In particular, the elongation to failure of the bare samples tested in SBF was increased by 126% with the application of the TiO_2 coating and by 223% with the ZrO_2 coating.

To quantify the SCC susceptibility of the bare and coated samples, the I_{UTS} and I_ε indices were evaluated and are reported in Fig. 10.

The application of 100 nm thick ZrO_2 coating is shown to be more effective in reducing the SCC susceptibility than the TiO_2 counterpart. In fact, the I_ε is reduced from 75.1 to 43.2 and to 18.3 applying the TiO_2 and ZrO_2 coating, respectively, while the I_{UTS} is reduced from 8.97 to 8.42 and 2.68 applying the TiO_2 and ZrO_2 coating, respectively. It is interesting to note that the impact on UTS is very low when applying the TiO_2 coating, whereas the impact on elongation is significant.

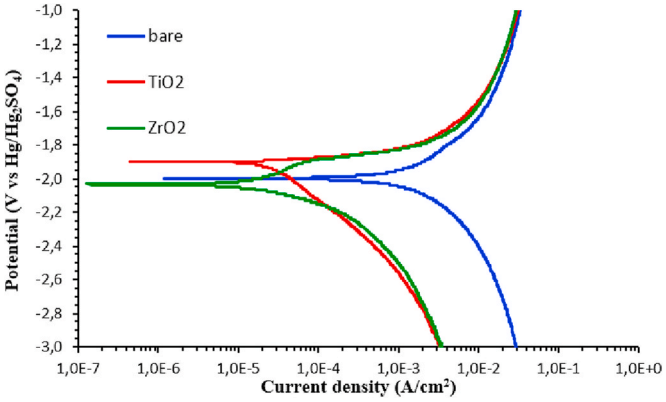

Fig. 7. Potentiodynamic polarization curves of bare (blue), TiO_2 coated (red) and ZrO_2 coated (green) AZ31 alloy in SBF.

Table 2
The results of corrosion potentials (E_{corr}) and corrosion current densities (i_{corr}) for bare and coated AZ31 samples in SBF.

	Bare	TiO_2 coating	ZrO_2 coating
E_{corr} (V)	−2.00 ± 0.02	−1.90 ± 0.01	−2.02 ± 0.01
i_{corr} (A/cm^2)	3.0 10^{-3} ± 0.4	2.5 10^{-5} ± 0.6	1.2 10^{-6} ± 0.3

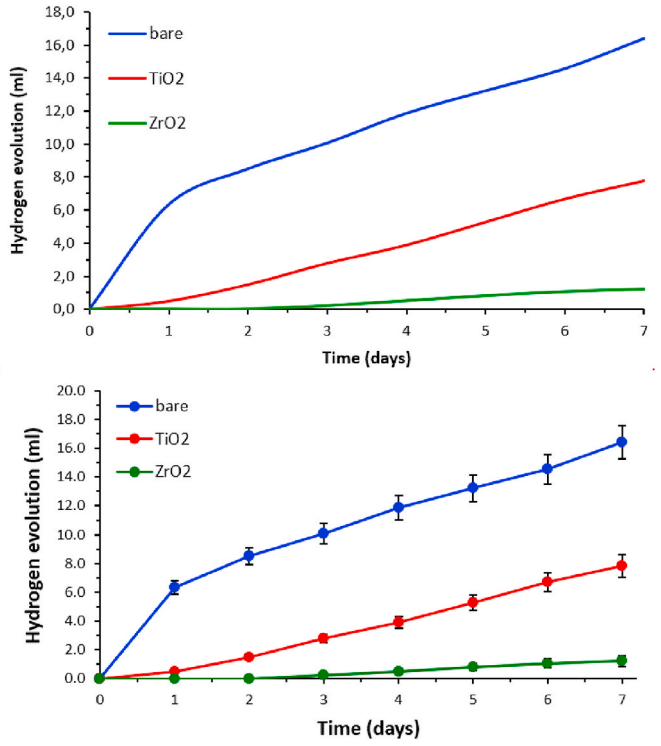

Fig. 8. Hydrogen evolved from the immersion of bare (blue), TiO_2 coated (red) and ZrO_2 coated (green) AZ31 alloy in SBF.

3.5. Fractography

Fracture surfaces of the bare samples tested in air and in SBF are reported in Fig. 11a and 11b and Fig. 11c and 11d, respectively. The overall view of the fracture surface confirms the ductile nature of the failure in the case of testing in air. Here, the fracture surface is characterized by a significant number of dimples (Fig. 11a and 11b), while the sample tested in SBF shows mixed mode fracture features, namely ductile and brittle fracture characteristics. In addition, the surface

Table 3
Mechanical properties of bare and coated samples from Fig. 9.

Surface	In Air		In SBF	
	UTS (MPa)	Elongation at failure (%)	UTS (MPa)	Elongation at failure (%)
Bare	256.3 ± 8.7	24.5 ± 0.7	233.3 ± 1.9	6.1 ± 0.3
TiO_2 Coated	252.7 ± 5.2	24.3 ± 0.6	231.4 ± 5.1	13.8 ± 0.4
ZrO_2 Coated	253.6 ± 5.6	24.1 ± 0.5	246.8 ± 1.0	19.7 ± 0.2

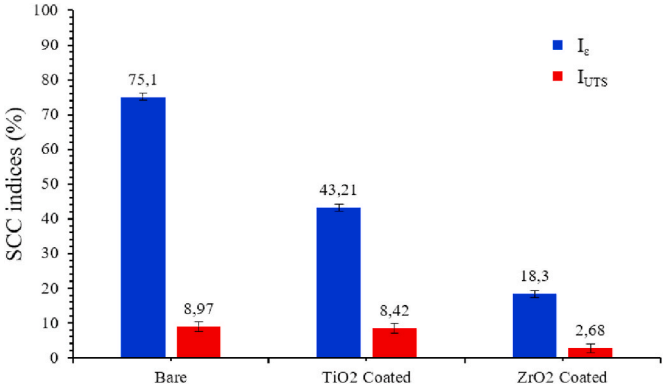

Fig. 10. SCC indices for the bare and coated AZ31 samples.

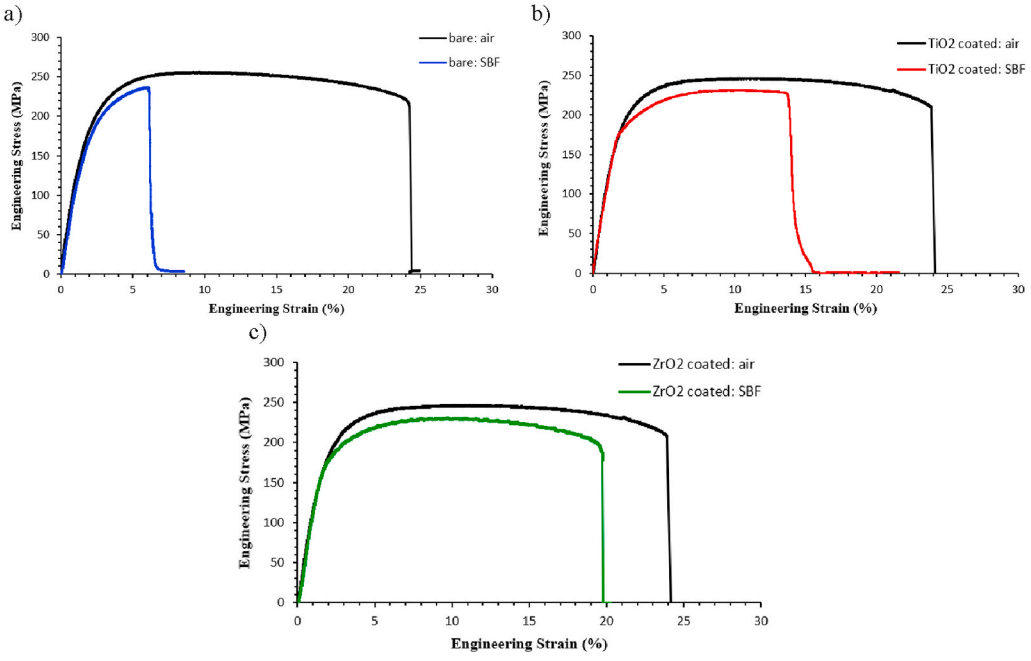

Fig. 9. Engineering stress-strain curves of bare (a) and coated (b) AZ31 samples tested in air and SBF at 37 °C and strain rate of 3.5·10^{-6} s^{-1}

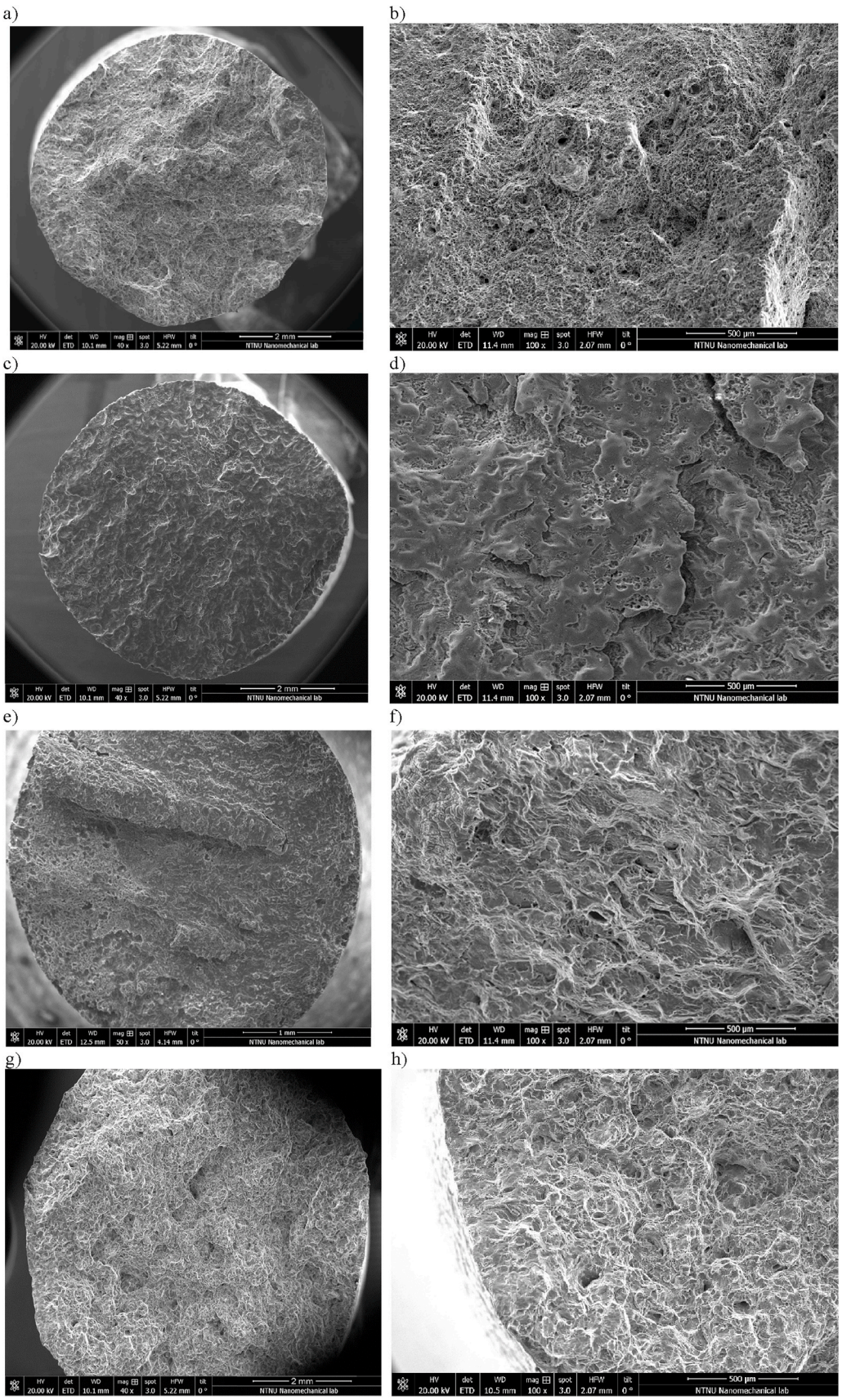

Fig. 11. Fracture surfaces of bare samples tested in air (a and b) and in SBF (c and d), of TiO_2 coated samples tested in SBF (e and f) and of ZrO_2 coated samples tested in SBF (g and h).

fracture appearance is completely different: in the case of SBF condition, both transgranular and intergranular cracks are evident, with a predominance of the former, which are absent in the case of air testing (compare Fig. 11d with Fig. 11b). The application of the coatings did not alter the AZ31 response mechanisms to SCC, being the fracture characterized by both a ductile and brittle zone, with the latter characterized by the presence of both intergranular and transgranular cracks. However, the application of the TiO_2 coating leads to the change of the fracture appearance in the brittle zone due to the reduced embrittlement of the material as a consequence of the reduced corrosion: in fact, while in the bare samples, the transgranular fracture was predominant, the TiO_2 coated samples show intergranular cracking as the main mechanism (Fig. 11f). Finally, the application of the ZrO_2 coating leads to a failure that is predominantly ductile (Fig. 11g). This is particularly apparent in the center of the sample, with the mixed mode fracture features close to the sample edges appearing to have experienced transgranular and intergranular cracking (Fig. 11h).

The reduced corrosion of the coated samples tested in SBF with respect to the bare sample is also confirmed by the tilted views of the gauge section (compare Fig. 12b and c with Fig. 12a), where deep secondary cracks and some pits can be observed in the bare samples, while no deep secondary cracks and no pits are present in the coated sample. In addition, necking can also be observed in the ZrO_2 coated samples confirming the increased ductility (Fig. 12c).

4. Discussions

An adequate resistance to cracking under the simultaneous action of a physiologically relevant corrosive environment and mechanical load is a fundamental requirement for an implant material. For Mg and its alloys, SCC is particularly relevant representing one of the main limitations for their acceptance as implant material (Winzer et al., 2007). Specifically, the high electrochemical activity of Mg must be reduced without changing its bulk properties, its surface characteristics and ability to degrade, even under mechanical stress. Here, a mechanically stable, ultrathin conformal and dense coating of a material with high electrochemical barrier is required. 100 nm ALD TiO_2 and ZrO_2 coated AZ31 alloys showed already significant reduction in i_{corr} by two (Marin et al., 2012) and three (Liu et al., 2018) orders of magnitude, respectively. However, is such an approach viable to reduce the SCC susceptibility, namely an increase in elongation to failure and UTS when tested in a physiologically relevant corrosive environment? Is the reduction in susceptibility related to the electrochemical barrier of the coating only?

Our 100 nm ALD TiO_2 and ZrO_2 coated AZ31 samples were subjected to SSRT at a strain rate of $3.5{\cdot}10^{-6}$ s^{-1} in SBF at 37 °C. Both coatings improve the SCC resistance (Figs. 9 and 10), their performances, however, vastly differ. While TiO_2 reduced the I_{UTS} and the I_ε by 6% and 40%, respectively, ZrO_2 reduced the I_{UTS} and the I_ε by 70% and 76%, respectively. The general SCC behavior of Mg alloys can be attributed to the combination of two mechanisms; (1) the anodic dissolution and (2) the cleavage-like fracture due to hydrogen embrittlement (HE) (Winzer et al., 2005). The rupture of the protective native $Mg(OH)_2$ film through anodic dissolution or mechanical loads allows evolved hydrogen from the corrosion process to enter into the matrix, thereby embrittling the material ultimately leading to premature fracture (Jafari et al., 2015). Altering the corrosion rate hence affects the SCC susceptibility directly. In particular, the lower the corrosion rate, the lower the SCC susceptibility due to a reduced effect of the anodic dissolution and of the HE. Therefore, the reduced SCC susceptibility of the coated samples can be explained directly with the corrosion performances of the coatings (Figs. 7 and 8). The i_{corr} of the bare samples is reduced by two and three orders of magnitude with the TiO_2 and ZrO_2 coatings, consistent with previous reports (Marin et al., 2012; Liu et al., 2018; Yang et al., 2017).

The highest impact in corrosion reduction can however be seen by the evolved hydrogen: from the bare samples it is reduced by 52% and 93% for TiO_2 and ZrO_2 coatings, respectively. Regarding the drastic decrease in I_ε, the lower embrittlement of the material can be directly linked to the reduced amount of evolved hydrogen. This is shown by the mechanical tests (Fig. 9), the fractographies of the samples tested in SBF (Fig. 11) and by the tilted view of the gauge section (Fig. 12). The TiO_2 coated samples are characterized by a brittle fracture zone, where the intergranular fracture, characteristic of the anodic dissolution, is predominant (Fig. 11b). This is different from the bare samples, where the transgranular fracture related to the HE phenomenon is predominant (Fig. 11a). We can thus conclude that a lower amount of hydrogen entering the material with the application of the coating decreases its SCC susceptibility. Further improvements are achieved by applying ZrO_2

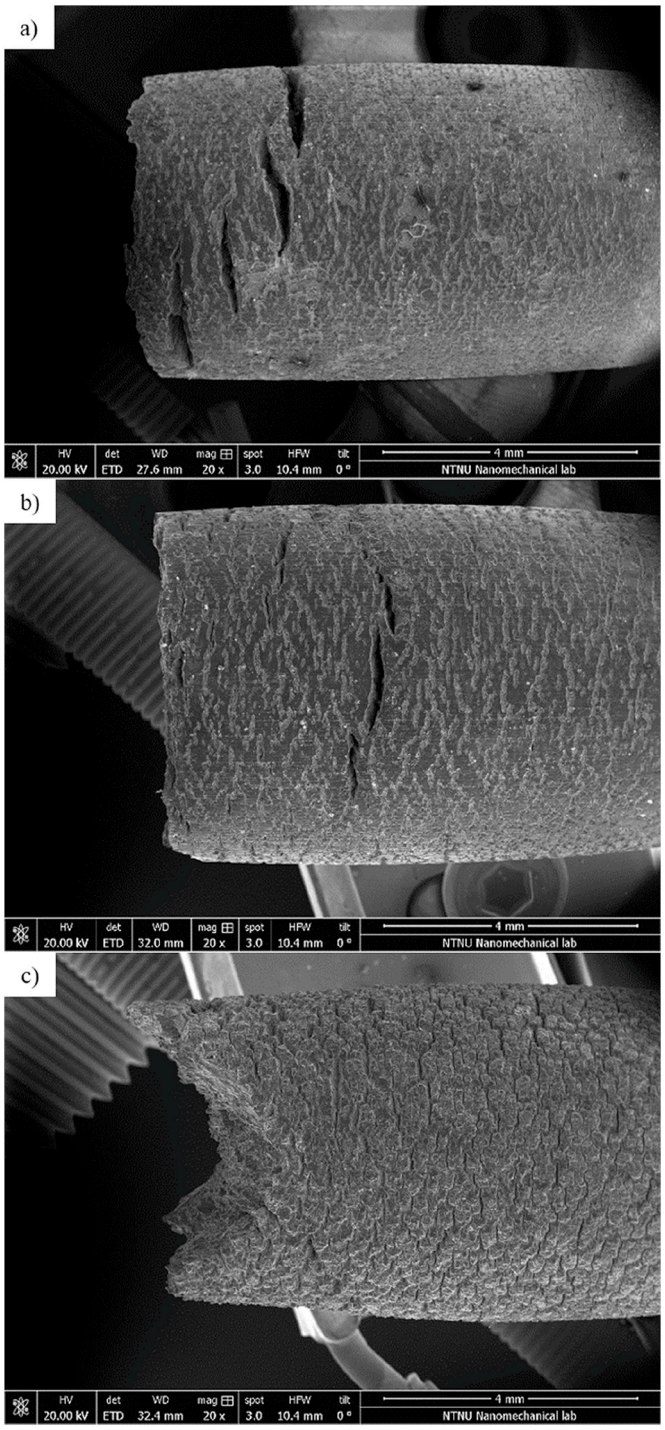

Fig. 12. SEM fractographies of the gauge section of bare (a), of TiO_2 coated (b) and of ZrO_2 coated (c) AZ31 samples after SSRTs in SBF.

coatings. Here, the fracture behavior changes from predominantly cleavage facets towards a mixed brittle-ductile behavior where cleavage facets and dimple-like morphologies are present (Fig. 11c). The increased ductility is confirmed by the tilted views of the gauge section of ZrO_2 coated samples (Fig. 12c), where necking can be observed. Figs. 12b and 12c shows that pitting was significantly reduced with respect to the bare sample (Fig. 12a). This hints towards the conformality of the coating protecting all cavities on the surface of the sample. As pitting is known as the main precursor for SCC crack initiation (Stampella et al., 1984; Raja and Padekar, 2013), this reduced tendency represents another important reason for the reduced SCC susceptibility.

Electrochemical stability can explain the different corrosion performances of the TiO_2 and ZrO_2 coatings. ZrO_2 is electrochemically more stable than TiO_2 due to its higher cohesive energy (Turchanin and Agraval, 2008). A higher cohesive energy makes a material more electrochemically stable and lowers its corrosion (Li and Li, 2006). In addition, TiO_2 is also reported to be more hydrophilic than ZrO_2, thus leading to a higher corrosion rate in aqueous solutions (Akaltun et al., 2016). Miyauchi et al. reported in fact TiO_2 to have a water contact angle of around 55° (Miyauchi et al., 2002), while Gonzalez-Martin et al. reported ZrO_2 to have a water contact angle of around 70° (González-Martín et al., 1999).

Furthermore, the integrity of the coating is another important aspect. Defects such as pores and cracks provide a path for the fluid to access the substrate. More and longer cracks are observed on the TiO_2 coated sample (Fig. 6 and Table 1) compared to the ZrO_2 coated counterpart, which may further explain the drastic difference in corrosion behavior. A comparison to the corrosion rate of bulk TiO_2 and ZrO_2 helps to explain the influence of the observed defects. According to Faraday's law (Pardo et al., 2010), bulk TiO_2 and ZrO_2 corrodes at a rate equal to $0.37{\cdot}10^{-6}$ and $0.87{\cdot}10^{-7}$ mm/year, respectively (Lorenzetti et al., 2014; Sowa et al., 2017), when exposed to simulated body fluid at 37 °C. However, we experience much higher corrosion rates; $2.11{\cdot}10^{-4}$ and $1.14{\cdot}10^{-5}$ mm/year, respectively, rates that are 570 and 130 times higher, confirming the lower defectiveness in ZrO_2 coated samples. Defects usually form as cracks as a consequence of the induced residual stresses on the coating due to the difference in the thermal expansion coefficient between the coating and the substrate (Il Pyun et al., 1993; ((Christoph Leyens and ManfredPetersJohn Wiley and Sons, 2003))). The coefficient of thermal expansion of Mg is $27{\cdot}10^{-6}$ °C^{-1} (Yang et al., 2011), that of ZrO_2 is $11{\cdot}10^{-6}$ °C^{-1} and that of TiO_2 is $7{\cdot}10^{-6}$ °C^{-1} (Hayashi et al., 2005; Hummer et al., 2007). Hence, the lower number of defects in ZrO_2 with respect to TiO_2 coatings may be attributed to its closer match in the coefficient of thermal expansion to the substrate.

Finally, the difference in the coating's mechanical properties can further influence the SCC susceptibility. ZrO_2 has a higher UTS and higher elongation to failure compared to TiO_2, eventually resisting higher strains without rupture (Cristache et al., 2011; Titanium Dioxide - online). We hypothesize that the longer the coating layer resists to the applied stresses, the longer the barrier effect of the coating will last, which directly affects the SCC behaviour.Whereas the drastic reduction of the SCC susceptibility indices I_ε and I_{UTS} show the potential to render ALD coated AZ31 materials interesting for biomedical applications, our results also show the importance of choosing a proper coating material. A wide range of factors, including the cohesive energy, the wettability and the thermal expansion mismatch of the coating with respect to the substrate must be considered. Further, we indicate the fundamental role of the mechanical characteristics of the protective layer for tailoring the SCC behaviour. A high elongation to failure may guarantee the coating's integrity when strained.

5. Conclusion

In this study, the effect of a 100 nm thick TiO_2 and ZrO_2 coatings on the SCC susceptibility of the AZ31 Mg alloy was assessed. Slow strain rate tests (SSRTs) at a strain rate of $3.5{\cdot}10^{-6}$ s^{-1} were carried out in Simulated Body Fluid (SBF) at 37 °C on bare and coated samples, respectively. In addition, potentiodynamic polarization tests, hydrogen evolution tests and fracture surfaces analyses were carried out.

The main findings can be summarized as follows:

- Both coatings reduce the SCC susceptibility of AZ31 alloy. TiO_2 reduced the I_{UTS} and the I_ε of 6% and 40%, respectively, while ZrO_2 of 70% and 76%, respectively. The fracture surface analyses showed a transition from a mixed mode fracture where the brittle zone was predominantly transgranular in the bare samples, to a predominance of intergranular failures in the TiO_2 coated samples and to a predominantly ductile failure for ZrO_2 coated samples.
- The different SCC susceptibility was attributed to the improved corrosion of the coated samples. The difference in the corrosion behavior between TiO_2 and ZrO_2 coated samples was related to the four main aspects, i.e. the different cohesive energies, wettabilities, defect densities and sizes as well as mechanical properties. With a comparably higher cohesive energy, ZrO_2 coatings are less prone to corrosion and are also characterized by a lower wettability. Moreover, a lower mismatch between the coefficient of thermal expansion of ZrO_2 and Mg with respect to that between TiO_2 and Mg reduced the number of defects providing a more stable barrier to the fluid. Finally, ZrO_2 has a higher UTS and higher ε_f compared to TiO_2, which increases its stability when mechanically stressed, hindering the fluid's access to the base material, even under strained conditions.

This work shows that all factors - cohesive energy, wettability, thermal expansion and elongation at break of the coating are important parameters to be considered when designing an effective corrosion barrier for biomedical Mg alloys that are subject to mechanical loads.

CRediT authorship contribution statement

M. Peron: Conceptualization, Data curation, Investigation, Methodology, Validation, Visualization, Writing - original draft, Writing - review & editing. **A. Bin Afif:** Data curation, Investigation, Validation. **A.L. Dadlani:** Data curation, Investigation, Validation. **F. Berto:** Supervision. **J. Torgersen:** Supervision, Writing - original draft, Writing - review & editing.

Declaration of competing interest

The authors declare that they have no known competing interests or personal relationships that could have appeared to influence the work reported in this pap

Acknowledgement

Abdulla Bin Afif was supported by NTNU's Enabling technologies: Nanotechnology. The Research Council of Norway is acknowledged for the support to the Norwegian Micro- and Nano-Fabrication Facility, NorFab, project number 245963/F50. Anup Lal Dadlani was funded by the Norwegian Research Council under project number 274459 Translate.

References

Akahori, T., Niinomi, M., Fukunaga, K.-I., Inagaki, I., 2000. Effects of microstructure on the short fatigue crack initiation and propagation characteristics of biomedical α/β titanium alloys. Metall. Mater. Trans. 31, 1949–1958. https://doi.org/10.1007/s11661-000-0222-z.

Akaltun, Y., Aslan, M., Yetim, T., Çayir, T., Çelik, A., 2016. The effect of wettability on corrosion resistance of oxide films produced by SILAR method on magnesium, aluminum and copper substrates. Surf. Coating. Technol. 292, 121–131. https://doi.org/10.1016/j.surfcoat.2016.03.011.

Antunes, R.A., de Oliveira, M.C.L., 2012. Corrosion fatigue of biomedical metallic alloys: mechanisms and mitigation. Acta Biomater. 8, 937–962. https://doi.org/10.1016/j.actbio.2011.09.012.

ASTM International, ASTM-E466-96. Standard practice for slow strain rate testing to evaluate the susceptibility of metallic materials to environmentally assisted cracking. n.d. https://doi.org/10.1520/G0129-00R13.

Bauer, T.W., Schils, J., 1999. The pathology of total joint arthroplasty.II. Mechanisms of implant failure. Skeletal Radiol. 28, 483–497. http://www.ncbi.nlm.nih.gov/pubmed/10525792. (Accessed 31 March 2017).

Beech, I.B., Sunner, J.A., Arciola, C.R., Cristiani, P., 2006. Microbially-influenced corrosion: damage to prostheses, delight for bacteria. Int. J. Artif. Organs 29, 443–452. http://www.ncbi.nlm.nih.gov/pubmed/16705614. (Accessed 20 June 2017).

Bobby Kannan, M., Dietzel, W., Blawert, C., Atrens, A., Lyon, P., 2008. Stress corrosion cracking of rare-earth containing magnesium alloys ZE41, QE22 and Elektron 21 (EV31A) compared with AZ80. Mater. Sci. Eng. 480, 529–539. https://doi.org/10.1016/J.MSEA.2007.07.070.

Cai, D.G., Bao, M.M., Wang, X.Y., Yang, L., Qin, G.W., Wang, R.X., Chen, D.F., Zhang, E. L., 2019. Biocorrosion properties of Ti–3Cu alloy in F ion-containing solution and acidic solution and biocompatibility. Rare Met. 38, 503–511. https://doi.org/10.1007/s12598-019-01202-9.

Chalker, P.R., 2016. Photochemical atomic layer deposition and etching. Surf. Coating. Technol. 291, 258–263. https://doi.org/10.1016/j.surfcoat.2016.02.046.

Chen, L., Sheng, Y., Zhou, H., Li, Z., Wang, X., Li, W., 2018. Influence of a MAO + PLGA coating on biocorrosion and stress corrosion cracking behavior of a magnesium alloy in a physiological environment. Corrosion Sci. 148, 134–143. https://doi.org/10.1016/J.CORSCI.2018.12.005.

Choudhary, L., Singh Raman, R.K., Hofstetter, J., Uggowitzer, P.J., 2014. In-vitro characterization of stress corrosion cracking of aluminium-free magnesium alloys for temporary bio-implant applications. Mater. Sci. Eng. C 42, 629–636. https://doi.org/10.1016/J.MSEC.2014.06.018.

(Christoph) Leyens, C., (Manfred) Peters, M., John Wiley & Sons, 2003. Wiley InterScience (Online Service), Titanium and Titanium Alloys : Fundamentals and Applications. Wiley-VCH.

Cremers, V., Puurunen, R.L., Dendooven, J., 2019. Conformality in atomic layer deposition: current status overview of analysis and modelling. Appl. Phys. Rev. 6, 021302 https://doi.org/10.1063/1.5060967.

Cristache, C.M., Burlibasa, M., Cristache, G., Drafta, S., Popovici, I.A., Iliescu, A.A., Zisi, S., Burlibasa, L., 2011. Zirconia and its biomedical applications. Metal. Int XVI, 18–23. https://www.researchgate.net/publication/286038141_Zirconia_and_its_biomedical_applications. (Accessed 20 January 2020).

Dujovne, A.R., Bobyn, J.D., Krygier, J.J., Miller, J.E., Brooks, C.E., 1993. Mechanical compatibility of noncemented hip prostheses with the human femur. J. Arthroplasty 8, 7–22. https://doi.org/10.1016/S0883-5403(06)80102-6.

Engh, C.A., Bobyn, J.D., 1988. The influence of stem size and extent of porous coating on femoral bone resorption after primary cementless hip arthroplasty. Clin. Orthop. Relat. Res. 7–28. http://www.ncbi.nlm.nih.gov/pubmed/3370887. (Accessed 31 March 2017).

Ginebra, M.P., Traykova, T., Planell, J.A., 2006. Calcium phosphate cements as bone drug delivery systems: a review. J. Contr. Release 113, 102–110. https://doi.org/10.1016/j.jconrel.2006.04.007.

González-Martín, M.L., Labajos-Broncano, L., Jańczuk, B., Bruque, J.M., 1999. Wettability and surface free energy of zirconia ceramics and their constituents. J. Mater. Sci. 34, 5923–5926. https://doi.org/10.1023/A:1004767914895.

Graniel, O., Weber, M., Balme, S., Miele, P., Bechelany, M., 2018. Atomic layer deposition for biosensing applications. Biosens. Bioelectron. 122, 147–159. https://doi.org/10.1016/J.BIOS.2018.09.038.

Hänzi, A.C., Sologubenko, A.S., Uggowitzer, P.J., 2009. Design strategy for new biodegradable Mg–Y–Zn alloys for medical applications. Int. J. Mater. Res. 100, 1127–1136. https://doi.org/10.3139/146.110157.

H. Harianawala, M. Kheur, S. Kheur, T. Sethi, A. Bal, M. Burhanpurwala, F. Sayed, Biocompatibility of Zirconia, n.d.

Hayashi, H., Saitou, T., Maruyama, N., Inaba, H., Kawamura, K., Mori, M., 2005. Thermal expansion coefficient of yttria stabilized zirconia for various yttria contents. Solid State Ionics 176, 613–619. https://doi.org/10.1016/j.ssi.2004.08.021.

Hou, S.S., Zhang, R.R., Guan, S.K., Ren, C.X., Gao, J.H., Lu, Q.B., Cui, X.Z., 2012. In vitro corrosion behavior of Ti-O film deposited on fluoride-treated Mg–Zn–Y–Nd alloy. Appl. Surf. Sci. 258, 3571–3577. https://doi.org/10.1016/J.APSUSC.2011.11.116.

http://share.iofbonehealth.org/EU-6-Material/Reports/IOF%20Report_EU.pdf, (n.d.). http://share.iofbonehealth.org/EU-6-Material/Reports/IOF Report_EU.pdf (accessed November 20, 2019).

Huang, L., Su, K., Zheng, Y.F., Yeung, K.W.K., Liu, X.M., 2019. Construction of TiO2/silane nanofilm on AZ31 magnesium alloy for controlled degradability and enhanced biocompatibility. Rare Met. 38, 588–600. https://doi.org/10.1007/s12598-018-1187-7.

Hummer, D.R., Heaney, P.J., Post, J.E., 2007. Thermal expansion of anatase and rutile between 300 and 575 K using synchrotron powder X-ray diffraction. Powder Diffr. 22, 352–357. https://doi.org/10.1154/1.2790965.

Il Pyun, S., Yoon, Y.G., Lugscheider, E., Mathesius, R., 1993. Relationship between interfacial reaction and adhesion at PVD TiO2 film-metal (Ti or Al) interfaces. Surf. Coating. Technol. 61, 233–237. https://doi.org/10.1016/0257-8972(93)90231-C.

Jacobs, J.J., Gilbert, J.L., Urban, R.M., 1998. Corrosion of metal orthopaedic implants. J. Bone Joint Surg. Am. 80, 268–282. http://www.ncbi.nlm.nih.gov/pubmed/9486734. (Accessed 31 March 2017).

Jacobs, J.J., Hallab, N.J., Skipor, A.K., Urban, R.M., 2003. Metal degradation products: a cause for concern in metal-metal bearings? Clin. Orthop. Relat. Res. 139–147. https://doi.org/10.1097/01.blo.0000096810.78689.62.

Jafari, S., Harandi, S.E., Singh Raman, R.K., 2015. A review of stress-corrosion cracking and corrosion fatigue of magnesium alloys for biodegradable implant applications. Jom 67, 1143–1153. https://doi.org/10.1007/s11837-015-1366-z.

Jafari, S., Raman, R.K.S., Davies, C.H.J., Hofstetter, J., Uggowitzer, P.J., Löffler, J.F., 2017. Stress corrosion cracking and corrosion fatigue characterisation of MgZn1Ca0.3 (ZX10) in a simulated physiological environment. J. Mech. Behav. Biomed. Mater. 65, 634–643. https://doi.org/10.1016/J.JMBBM.2016.09.033.

Jafari, S., Raman, R.K.S., Davies, C.H.J., 2018. Stress corrosion cracking of an extruded magnesium alloy (ZK21) in a simulated body fluid. Eng. Fract. Mech. 201, 47–55. https://doi.org/10.1016/J.ENGFRACMECH.2018.09.002.

Kannan, M.B., Raman, R.K.S., 2008. In vitro degradation and mechanical integrity of calcium-containing magnesium alloys in modified-simulated body fluid. Biomaterials 29, 2306–2314. https://doi.org/10.1016/J.BIOMATERIALS.2008.02.003.

Kasuga, T., Kondo, H., Nogami, M., 2002. Apatite formation on TiO2 in simulated body fluid. J. Cryst. Growth 235, 235–240. https://doi.org/10.1016/S0022-0248(01)01782-1.

Kerner, J., Huiskes, R., van Lenthe, G.H., Weinans, H., van Rietbergen, B., Engh, C.A., Amis, A.A., 1999. Correlation between pre-operative periprosthetic bone density and post-operative bone loss in THA can be explained by strain-adaptive remodelling. J. Biomech. 32, 695–703. https://doi.org/10.1016/S0021-9290(99)00041-X.

Kim, J.H., Lee, S., Im, H.S., 1999. Effect of target density and its morphology on TiO2 thin films grown on Si(100) by PLD. Appl. Surf. Sci. 151, 6–16. https://doi.org/10.1016/S0169-4332(99)00269-X.

Kokubo, T., Takadama, H., 2006. How useful is SBF in predicting in vivo bone bioactivity? Biomaterials 27, 2907–2915. https://doi.org/10.1016/J.BIOMATERIALS.2006.01.017.

Lei, T., 2015. Anodic electrodeposition of MgO coatings to improve corrosion resistance in vivo. In: Surf. Modif. Magnes. Its Alloy. Biomed. Appl. Elsevier Inc., pp. 135–150. https://doi.org/10.1016/B978-1-78242-078-1.00006-2

Li, Q., 2013. Sol-gel coatings to improve the corrosion resistance of magnesium (Mg) alloys. In: Corros. Prev. Magnes. Alloy. Woodhead Publ. Ser. Met. Surf. Eng., Elsevier Ltd, pp. 469–485. https://doi.org/10.1533/9780857098962.3.469. A Vol.

Li, W., Li, D.Y., 2006. Influence of surface morphology on corrosion and electronic behavior. Acta Mater. 54, 445–452. https://doi.org/10.1016/j.actamat.2005.09.017.

Liu, F., Shan, D., Song, Y., Han, E.-H., Ke, W., 2011. Corrosion behavior of the composite ceramic coating containing zirconium oxides on AM30 magnesium alloy by plasma electrolytic oxidation. Corrosion Sci. 53, 3845–3852. https://doi.org/10.1016/J.CORSCI.2011.07.037.

Liu, X., Yang, Q., Li, Z., Yuan, W., Zheng, Y., Cui, Z., Yang, X., Yeung, K.W.K., Wu, S., 2018. A combined coating strategy based on atomic layer deposition for enhancement of corrosion resistance of AZ31 magnesium alloy. Appl. Surf. Sci. 434, 1101–1111. https://doi.org/10.1016/J.APSUSC.2017.11.032.

Lorenzetti, M., Pellicer, E., Sort, J., Baró, M.D., Kovač, J., Novak, S., Kobe, S., 2014. Improvement to the corrosion resistance of Ti-based implants using hydrothermally synthesized nanostructured anatase coatings. Materials (Basel) 7, 180–194. https://doi.org/10.3390/ma7010180.

Marin, E., Lanzutti, A., Guzman, L., Fedrizzi, L., 2012. Chemical and electrochemical characterization of TiO2/Al2O3 atomic layer depositions on AZ-31 magnesium alloy. J. Coating Technol. Res. 9, 347–355. https://doi.org/10.1007/s11998-011-9372-8.

Miyauchi, M., Kieda, N., Hishita, S., Mitsuhashi, T., Nakajima, A., Watanabe, T., Hashimoto, K., 2002. Reversible wettability control of TiO2 surface by light irradiation. Surf. Sci. 511, 401–407. https://doi.org/10.1016/S0039-6028(02)01551-0.

Mohajernia, S., Pour-Ali, S., Hejazi, S., Saremi, M., Kiani-Rashid, A.-R., 2018. Hydroxyapatite coating containing multi-walled carbon nanotubes on AZ31 magnesium: mechanical-electrochemical degradation in a physiological environment. Ceram. Int. 44, 8297–8305. https://doi.org/10.1016/J.CERAMINT.2018.02.015.

Nezar, S., Saoula, N., Sali, S., Faiz, M., Mekki, M., Laoufi, N.A., Tabet, N., 2017. Properties of TiO 2 thin films deposited by rf reactive magnetron sputtering on biased substrates. Appl. Surf. Sci. 395, 172–179. https://doi.org/10.1016/j.apsusc.2016.08.125.

Pardo, A., Feliu, S., Merino, M.C., Arrabal, R., Matykina, E., 2010. Electrochemical estimation of the corrosion rate of magnesium/aluminium alloys. Int. J. Corros. 2010 https://doi.org/10.1155/2010/953850.

Peron, M., Torgersen, J., Berto, F., 2017. Mg and its alloys for biomedical applications: exploring corrosion and its interplay with mechanical failure. Metals (Basel) 7, 252. https://doi.org/10.3390/met7070252.

Peron, M., Torgersen, J., Berto, F., 2019a. Effect of Zirconia ALD coating on stress corrosion cracking of AZ31 alloy in simulated body fluid. In: Procedia Struct. Integr. Elsevier B.V., pp. 538–548. https://doi.org/10.1016/j.prostr.2019.08.198

Peron, M., Berto, F., Torgersen, J., 2019b. Stress corrosion cracking behavior of zirconia ALD–coated AZ31 alloy in simulated body fluid. Mater. Des. Process. Commun. 126. https://doi.org/10.1002/mdp2.126 mdp.2.

Peron, M., Bertolini, R., Ghiotti, A., Torgersen, J., Bruschi, S., Berto, F., 2020a. Enhancement of stress corrosion cracking of AZ31 magnesium alloy in simulated body fluid thanks to cryogenic machining. J. Mech. Behav. Biomed. Mater. 101, 103429. https://doi.org/10.1016/J.JMBBM.2019.103429.

Peron, M., Berto, F., Torgersen, J., 2020b. Magnesium and its Alloys as Implant Materials : Corrosion, Mechanical and Biological Performances. CRC Press LLC.

Peron, M., Skaret, P.C., Fabrizi, A., Varone, A., Montanari, R., Roven, H.J., Ferro, P., Berto, F., Torgersen, J., 2020c. The effect of Equal Channel Angular Pressing on the stress corrosion cracking susceptibility of AZ31 alloy in simulated body fluid. J. Mech. Behav. Biomed. Mater. 103724. https://doi.org/10.1016/j.jmbbm.2020.103724.

Peron, M., Bin Afif, A., Dadlani, A., Berto, F., Torgersen, J., 2020d. Comparing physiologically relevant corrosion performances of Mg AZ31 alloy protected by ALD and sputter coated TiO2. Surf. Coating. Technol. 125922. https://doi.org/10.1016/j.surfcoat.2020.125922.

Pound, B.G., 2014a. Corrosion behavior of metallic materials in biomedical applications. I . Ti and its alloys 32, 1–20. https://doi.org/10.1515/corrrev-2014-0007.

Pound, B.G., 2014b. Corrosion behavior of metallic materials in biomedical applications. II . Stainless steels and Co-Cr alloys 32, 21–41. https://doi.org/10.1515/corrrev-2014-0008.

Qi, Z.-R., Zhang, Q., Tan, L.-L., Lin, X., Yin, Y., Wang, X.-L., Yang, K., Wang, Y., 2014. Comparison of degradation behavior and the associated bone response of ZK60 and PLLA in vivo. J. Biomed. Mater. Res. 102, 1255–1263. https://doi.org/10.1002/jbm.a.34795.

Raja, V.S., Padekar, B.S., 2013. Role of chlorides on pitting and hydrogen embrittlement of Mg–Mn wrought alloy. Corrosion Sci. 75, 176–183. https://doi.org/10.1016/J.CORSCI.2013.05.030.

L. Rimondini, L. Cerroni, A. Carrassi, P. Torricelli, Bacterial colonization of zirconia ceramic surfaces: an in vitro and in vivo study., Int. J. Oral Maxillofac. Implants 17 (n.d.)793–8. http://www.ncbi.nlm.nih.gov/pubmed/12507238 (accessed January 23, 2020).

Singh Raman, R.K., Jafari, S., Harandi, S.E., 2015. Corrosion fatigue fracture of magnesium alloys in bioimplant applications: a review. Eng. Fract. Mech. 137, 97–108. https://doi.org/10.1016/j.engfracmech.2014.08.009.

Smith, M.F., 2007. Comparing cold spray with thermal spray coating technologies. In: Cold Spray Mater. Depos. Process Fundam. Appl. Elsevier Ltd., pp. 43–61. https://doi.org/10.1533/9781845693787.1.43

Song, G., 2007. Control of biodegradation of biocompatable magnesium alloys. Corrosion Sci. 49, 1696–1701. https://doi.org/10.1016/J.CORSCI.2007.01.001.

Song, G., Atrens, A., StJohn, D., 2013. An hydrogen evolution method for the estimation of the corrosion rate of magnesium alloys. In: Magnes. Technol. 2001. John Wiley & Sons, Inc., Hoboken, NJ, USA, pp. 254–262. https://doi.org/10.1002/9781118805497.ch44.

Sonia, T.A., Sharma, C.P., 2014. Polymers in oral insulin delivery. In: Oral Deliv. Insul. Elsevier, pp. 257–310. https://doi.org/10.1533/9781908818683.257.

Sowa, M., Łastówka, D., Kukharenko, A.I., Korotin, D.M., Kurmaev, E.Z., Cholakh, S.O., Simka, W., 2017. Characterisation of anodic oxide films on zirconium formed in sulphuric acid: XPS and corrosion resistance investigations. J. Solid State Electrochem. 21, 203–210. https://doi.org/10.1007/s10008-016-3369-2.

Staiger, M.P., Pietak, A.M., Huadmai, J., Dias, G., 2006. Magnesium and its alloys as orthopedic biomaterials: a review. Biomaterials 27, 1728–1734. https://doi.org/10.1016/j.biomaterials.2005.10.003.

Stampella, R.S., Procter, R.P.M., Ashworth, V., 1984. Environmentally-induced cracking of magnesium. Corrosion Sci. 24, 325–341. https://doi.org/10.1016/0010-938X(84)90017-9.

Sumner, D.R., Galante, J.O., 1992. Determinants of stress shielding: design versus materials versus interface. Clin. Orthop. Relat. Res. 202–212. http://www.ncbi.nlm.nih.gov/pubmed/1729005. (Accessed 31 March 2017).

Teoh, S., 2000. Fatigue of biomaterials: a review. Int. J. Fatig. 22, 825–837. https://doi.org/10.1016/S0142-1123(00)00052-9.

Thirumalaikumarasamy, D., Shanmugam, K., Balasubramanian, V., 2014. Comparison of the corrosion behaviour of AZ31B magnesium alloy under immersion test and potentiodynamic polarization test in NaCl solution. J. Magnes. Alloy. 2, 36–49. https://doi.org/10.1016/J.JMA.2014.01.004.

Titanium Dioxide - online catalogue source - supplier of research materials in small quantities - Goodfellow. n.d. http://www.goodfellow.com/E/Titanium-Dioxide.html. (Accessed 20 January 2020).

Turchanin, M.A., Agraval, P.G., 2008. Cohesive energy, properties, and formation energy of transition metal alloys. Powder Metall. Met. Ceram. 47, 26–39. https://doi.org/10.1007/s11106-008-0006-3.

Turner, T.M., Sumner, D.R., Urban, R.M., Igloria, R., Galante, J.O., 1997. Maintenance of proximal cortical bone with use of a less stiff femoral component in hemiarthroplasty of the hip without cement. An investigation in a canine model at six months and two years. J. Bone Joint Surg. Am. 79, 1381–1390. http://www.ncbi.nlm.nih.gov/pubmed/9314401. (Accessed 31 March 2017).

Uchida, M., Kim, H.-M., Kokubo, T., Nakamura, T., 1999. APATITE-FORMING ability OF titania gels with different structures. In: Bioceramics. WORLD SCIENTIFIC, pp. 149–152. https://doi.org/10.1142/9789814291064_0036.

Van Rietbergen, B., Huiskes, R., Weinans, H., Sumner, D.R., Turner, T.M., Galante, J.O., 1993. The mechanism of bone remodeling and resorption around press-fitted THA stems. J. Biomech. 26, 369–382. https://doi.org/10.1016/0021-9290(93)90001-U.

Wang, X.X., Hayakawa, S., Tsuru, K., Osaka, A., 2002. Bioactive titania gel layers formed by chemical treatment of Ti substrate with a H2O2/HCl solution. Biomaterials 23, 1353–1357. https://doi.org/10.1016/S0142-9612(01)00254-X.

Wang, J., Xu, J., Hopkins, C., Chow, D.H., Qin, L., 2020. Biodegradable magnesium-based implants in orthopedics—a general review and perspectives. Adv. Sci. 1902443. https://doi.org/10.1002/advs.201902443.

Winzer, N., Atrens, A., Song, G., Ghali, E., Dietzel, W., Kainer, K.U., Hort, N., Blawert, C., 2005. A critical review of the Stress Corrosion Cracking (SCC) of magnesium alloys. Adv. Eng. Mater. 7, 659–693. https://doi.org/10.1002/adem.200500071.

Winzer, N., Atrens, A., Dietzel, W., Song, G., Kainer, K.U., 2007. Stress corrosion cracking in magnesium alloys: characterization and prevention. JOM 59, 49–53. https://doi.org/10.1007/s11837-007-0104-6.

Wolff, J., 1986. The Law of Bone Remodelling. Springer Berlin Heidelberg, Berlin, Heidelberg. https://doi.org/10.1007/978-3-642-71031-5.

Yang, H., Huang, L., Zh, M., 2011. Hot forming characteristics of magnesium alloy AZ31 and three-dimensional FE modeling and simulation of the hot splitting spinning process. In: Magnes. Alloy. - Des. Process. Prop. InTech. https://doi.org/10.5772/13778.

Yang, Q., Yuan, W., Liu, X., Zheng, Y., Cui, Z., Yang, X., Pan, H., Wu, S., 2017. Atomic layer deposited ZrO2 nanofilm on Mg-Sr alloy for enhanced corrosion resistance and biocompatibility. Acta Biomater. 58, 515–526. https://doi.org/10.1016/J.ACTBIO.2017.06.015.

Yu, J., Zhao, X., Du, J., Chen, W., 2000. Preparation, microstructure and photocatalytic activity of the porous TiO2 anatase coating by sol-gel processing. J. Sol. Gel Sci. Technol. 17, 163–171. https://doi.org/10.1023/A:1008703719929.

Zhen, Z., Xi, T., Zheng, Y., Li, L., Li, L., 2014. Vitro study on Mg–Sn–Mn alloy as biodegradable metals. J. Mater. Sci. Technol. 30, 675–685. https://doi.org/10.1016/J.JMST.2014.04.005.